Stability of Fe-bearing hydrous phases and element partitioning in the system MgO–Al$_2$O$_3$–Fe$_2$O$_3$–SiO$_2$–H$_2$O in Earth's lowermost mantle

Hongsheng Yuan [a,*], Li Zhang [a,*], Eiji Ohtani [b], Yue Meng [c], Eran Greenberg [d], Vitali B. Prakapenka [d]

[a] Center for High Pressure Science and Technology Advanced Research (HPSTAR), Shanghai 201203, China
[b] Department of Earth Science, Graduate School of Science, Tohoku University, Sendai 980-8578, Japan
[c] HPCAT, X-Ray Science Division, Argonne National Laboratory, Argonne, IL 60439, USA
[d] Center for Advanced Radiation Sources, University of Chicago, Chicago, IL 60637, USA

ARTICLE INFO

ABSTRACT

We performed high pressure–temperature (*P-T*) experiments on a model composition of hydrous subducted slabs in the MgO–Al$_2$O$_3$–Fe$_2$O$_3$–SiO$_2$–H$_2$O system using laser-heated diamond anvil cells. The phase assemblages were characterized combining *in-situ* synchrotron X-ray diffraction and *ex-situ* transmission electron microscope techniques. The hydrous δ-phase AlOOH–FeOOH–MgSiO$_2$(OH)$_2$–SiO$_2$ coexists with bridgmanite (Bdg), post-perovskite (pPv), or both in a broad *P-T* range of 104–126 GPa and 1750–2500 K. The hydrous pyrite-type FeOOH$_x$ phase was observed *in-situ* over a *P-T* range of 112–123 GPa and 1750–2300 K, coexisting with the pPv phase. Chemical analysis on recovered samples showed that considerable amount of Fe$_2$O$_2$(OH)$_2$ (8–13 mol%) and SiO$_2$ (9–13 mol%) in the δ-phase does not reduce its thermal stability compared to the Al-endmember, indicating that the Fe-bearing δ-phase can transport water to the lowermost mantle along the mantle geotherm. In this hydrous system, we observed that Al depletion in both the Bdg and pPv phases can significantly reduce the width of the Bdg to pPv transition in contrast to a wide two-phase coexistence region in a dry Al-rich system. Meanwhile, the Fe enrichment in the pPv phase relative to the coexisting Bdg phase lowers the transition pressure to the depth of the D$''$ discontinuity. Accordingly, the depth and thickness of the Bdg to pPv transition in subducted basaltic crustal materials can explain the seismically detected D$''$ discontinuity. Partial melting could be triggered by dehydration of the Fe-bearing hydrous phases due to a steep temperature gradient at the core mantle boundary (CMB), and therefore the ultralow-velocity zones (ULVZs) might be the regions where partial melting occurs at the lowermost mantle.

© 2019 Elsevier B.V. All rights reserved.

1. Introduction

High-resolution seismic tomography images show that pieces of slab materials may penetrate into the lower mantle down to the CMB (Zhao, 2012). Through the subduction of hydrous components in slabs (Kárason and van der Hilst, 2000; van der Hilst, 1999), a certain amount of water can be transported into the Earth's lowermost mantle. The observation of ice-VII and hydrous ringwoodite (∼1 wt.% H$_2$O) as inclusions in sub-lithospheric diamonds provides direct evidence that the transition zone and shallow lower mantle are at least locally wet (Pearson et al., 2014; Tschauner et al., 2018). In the lower mantle region, water might

be stored in both hydrous phases and nominally anhydrous minerals (NAMs) (Ohtani, 2015). The composition and structure of the hydrous phases evolve with increasing depth. For instance, the hydrous phase D [MgSi$_2$O$_4$(OH)$_2$] transforms to the hydrous phase H [MgSiO$_2$(OH)$_2$] at pressures above 48 GPa (Nishi et al., 2014). On the other hand, the hydrous δ-AlOOH remains stable down to the CMB along the normal mantle geotherm (Duan et al., 2018; Ohtani et al., 2001; Sano et al., 2008). The hydrous phase H, δ-AlOOH, ε-FeOOH and CaCl$_2$-type SiO$_2$ all adopt the orthorhombic structure with the *Pnnm* space group under the *P-T* conditions of the deep lower mantle (DLM) and they may form solid solutions. The stability of these potential solid solutions needs to be further clarified in the DLM. Indeed, a wide composition range of the solid solutions, including AlOOH–MgSiO$_2$(OH)$_2$ (Ohira et al., 2014; Suzuki et al., 2000; Walter et al., 2015), AlOOH–MgSiO$_2$(OH)$_2$–SiO$_2$ (Ohira et al., 2014), and (Al,Fe)OOH (Kawazoe et al., 2017; Nishi et al., 2017), have been successfully synthesized via high *P-T* ex-

periments. In addition, ε-FeOOH transforms to cubic pyrite-type FeOOH$_x$ ($x < 1$) or FeOOH phase (py-phase) with a $Pa\overline{3}$ space group above 70 GPa, and it was therefore proposed to be a potential deep-water carrier with a higher density relative to the Preliminary Reference Earth Model (PREM) average density (Dziewonski and Anderson, 1981; Hu et al., 2016; Nishi et al., 2017). Zhang et al. (2018) further found a hexagonal hydrous phase (HH-phase) in (Fe,Al)OOH at 107–136 GPa and 2400 K, which can transform to the cubic py-phase at low T. According to the previous studies, the Al-depleted Bdg coexists with the Al-rich hydrous δ-phase in the MgO–Al$_2$O$_3$–SiO$_2$–H$_2$O system due to selective partitioning of Al into the δ-phase (Ohtani et al., 2018; Ohira et al., 2014; Walter et al., 2015). These results in the aluminous systems suggested that hydrous conditions can significantly change the element partitioning between the minerals in the DLM. Fe in a wide range of oxidation states is an important component in subduction slabs, but the effect of Fe on a hydrous DLM system has not been studied yet. In this study, an investigation in a hydrous Fe,Al-bearing system was carried out to evaluate the combined effect of Al and Fe on the mineralogy in a model composition of hydrous subducted slabs under the P-T conditions of DLM.

The Bdg to pPv transition in MgSiO$_3$ (Murakami, 2004; Oganov and Ono, 2004) may provide a valid explanation for the D$''$ discontinuity, where an increase in shear velocity of 1–2% was detected at a depth range of 200–400 km above the CMB with a sharp discontinuity (e.g. <30 km beneath the Cocos Plate, Lay, 2008). Existing *in-situ* X-ray diffraction (XRD) measurements indicated wide variations in both the depth and thickness of the Bdg to pPv transitions in the San Carlos olivine, pyrolitic, and mid-oceanic-ridge basaltic compositions (Grocholski et al., 2012). Both the pyrolitic composition and the Al-rich silicate compositions show a wide two-phase coexistence region measuring 400–600 km (25–30 GPa) in thickness, which suggests a lack of the seismic velocity contrast required for the sharp D$''$ discontinuity (Catalli et al., 2009; Grocholski et al., 2012; Sun et al., 2018). In contrast to a much thinner two-phase coexistence region in San Carlos olivine, the Al$_2$O$_3$ content in the Al-rich compositions significantly expands the Bdg to pPv transition boundary. Furthermore, the Bdg to pPv transition occurs at a much greater depth in pyrolite and San Carlos olivine compositions, where Fe is depleted in the Bdg/pPv phase through preferential partitioning of Fe into the coexisting ferropericlase (Fp), whereas the transition in Fe-rich Bdg/pPv phases in mid-oceanic-ridge basalt (MORB) compositions occurs at a shallower depth in better accord with the D$''$ discontinuity (Grocholski et al., 2012; Ohta et al., 2008). These results suggest that Fe enrichment in the silicate phase can lower the Bdg to pPv transition pressure to the depth where the D$''$ seismic velocity discontinuity is detected.

In this study, we performed high P-T experiments in laser-heated diamond anvil cells (DACs) in a pressure range of 104–126 GPa and a temperature range of 1750–2500 K. We used a synthetic Fe-bearing hydrous gel composed of 60 mol%MgSiO$_3$–30 mol%Al$_2$O$_3$–10 mol%Fe$_2$O$_3$ (referred to as MAFSH) and containing ~7 wt.% water and another Fe-free hydrous gel composed of 70 mol%MgSiO$_3$–30 mol%Al$_2$O$_3$ (referred to as MASH) and containing ~6 wt.% water as the starting materials. We investigated stability of the Fe-bearing hydrous phases, identified phase assemblages under the P-T conditions of DLM, and measured element partitioning through a combination of *in-situ* XRD and *ex-situ* transmission electron microscopy (TEM) analysis.
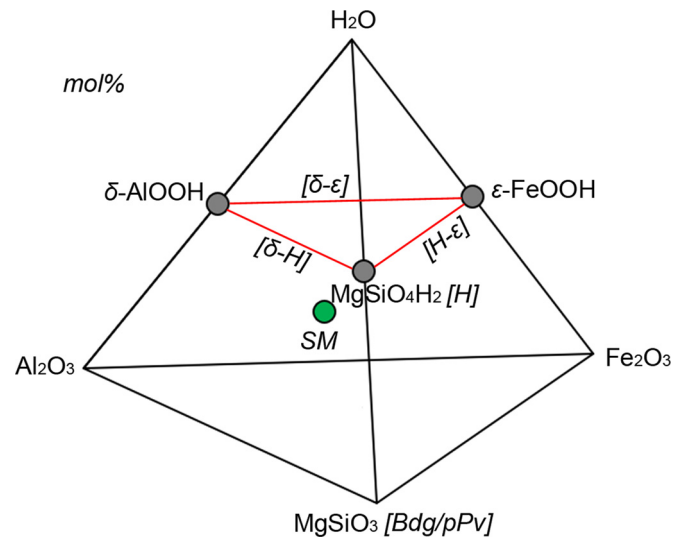
Fig. 1. The MAFSH quaternary with the compositions of the hydrous phases and the NAMs in the DLM. SM= starting material in this study. Tie lines of the δ-phase solid solutions are shown in red. (For interpretation of the colors in the figure(s), the reader is referred to the web version of this article.)

2. Experimental and analytical methods

2.1. Starting materials

Silicate gels were prepared according to the reported sol-gel procedure using reagent-grade Mg(NO$_3$)$_2$·6H$_2$O, Al(NO$_3$)$_3$·9H$_2$O, Fe(NO$_3$)$_3$·9H$_2$O, and (C$_2$H$_5$O)$_4$Si (Hamilton and Henderson, 1968) without further purification. The water content in the MAFSH composition was measured as 7.0(4) wt.% by the thermal gravimetric analysis (NETZSCH TG 209 F1 Libra®) up to 1000 °C. The homogeneity and composition ratio of this sample was examined by a scanning electron microscope (SEM) coupled with an energy dispersive X-ray spectroscopy (EDS) analysis (see Supporting Information, Fig. S1 and Table S1). The SEM-EDS results showed that the nitrogen and carbon content in the sample was beyond its detection limit, thus eliminating nitrogen or carbon contamination. The MAFSH quaternary with compositions of potential hydrous phases and NAMs in the DLM is shown in Fig. 1. The MASH composition was from the same batch that was used in a previous study by Ohira et al. (2014). We simplified the starting material with all iron in Fe^{3+} under the following considerations. First of all, significant amount of ferric iron is present in the Al-bearing Bdg, because the Fe^{3+} content of Bdg is coupled to Al concentration independent of oxygen fugacity in the lower mantle (Frost et al., 2004). Furthermore, existence of water produces an oxidized lower mantle region through redox reactions between water and iron/iron oxides, i.e., 4Fe + 2H$_2$O = 3FeH + FeOOH$_x$ (py-phase) and 4FeO + 2H$_2$O = FeH + 3FeOOH$_x$ (py-phase) (Mao et al., 2017; Yuan et al., 2018).

2.2. Sample loading and pressure determination

Boehler-Almax diamond anvils with flat culet diameters of 150 or 200 μm beveled at 10° up to 300 μm were used for the experiments. The MASH sample was mixed with ~10 wt.% Pt black as the laser absorber; no laser absorber was used for the MAFSH sample. The details of sample preparation are given in the Supporting Information and Fig. S2. We first drilled a recessed gasket with 40–50 μm in diameter using a laser drilling system. Then we placed a sample disk on the small step in the gasket with the sample surface parallel to the diamond culet and maintained space with 10 μm in thickness for Ne loading from both sides.

Compressed Ne was loaded, and then the sample was sandwiched between Ne layers. Ne was used as both a pressure transmitting medium and thermal insulating layers during laser heating for each experiment.

The pressures were determined based on the Mie–Grüneisen–Debye equation of state (EOS) of Ne reported by Dewaele et al. (2008). The unit-cell volume of Ne was determined by three diffraction peaks: (111), (200), and (220). To determine Ne pressures at high T, we picked the peak positions at the lower Bragg angle for each peak, which were attributed to the thermally expanded Ne in contact with the heated sample surface.

2.3. XRD experiments in laser-heated DACs

High P-T XRD experiments were performed at the High Pressure Collaborative Access Team (HPCAT) 16-ID-B beamline (Runs HS001, SH137, Sb029, Sb003 and Sa032) (Meng et al., 2015) and the GeoSoilEnviroCars 13-ID-D beamline (Runs S200u and SH172) (Prakapenka et al., 2008) at the Advanced Photon Source (APS), Argonne National Laboratory (Argonne, IL). The samples were heated using a double-sided heating technique with 1064-nm Ytterbium fiber lasers. The heating temperature was determined by fitting the visible portion of the gray-body radiation from both sides of the heated sample to the Planck radiation function, with an estimated temperature uncertainty of ±200 K throughout the heating experiments. We observed the appearance of all phases within two minutes of heating; a slight intensity change of the peaks occurred due to the increasing spottiness in the XRD patterns when the heating duration was extended to five minutes or longer, suggesting that our experiments were in equilibrium or very close to the equilibrium after the heating duration of five minutes. Therefore, we used a heating duration of five minutes for all the runs. Note that we did not conduct reversal runs for determining the precise Bdg to pPv phase boundaries in our experiments, because repeated heating might lead to phase segregation caused by thermally induced diffusion in DAC experiments.

At HPCAT, a heating spot size of approximately 35×35 μm^2 and an X-ray beam size of approximately 5×3 μm^2 were used (Meng et al., 2015), and angular dispersive XRD patterns were recorded on a MarCCD 165 detector. CeO$_2$ was used to calibrate the sample-to-detector distance at 1 bar. At GeoSoilEnviroCars, a flat-top laser heating spot size of approximately 10 μm in diameter and an X-ray beam size of approximately 3×4 μm^2 were used (Prakapenka et al., 2008), and angular dispersive XRD patterns were recorded on a Dectris Pilatus CdTe 1M pixel array detector for Run SH172 and on a Mar CCD 165 detector for Run S200u. LaB$_6$ was used to calibrate the sample-to-detector distance at 1 bar. Because of a relatively small heating spot was used at GeoSoilEnviroCars, we heated two separate spots on the sample in Run SH172, denoted as SH172-a and SH172-b.

We observed many overlapping peaks in a typical powder XRD pattern of the run products. To identify the phases and obtain their unit-cell parameters, we applied the multigrain XRD to sort out individual phases in the assemblage including a minor phase (Zhang et al., 2019, 2016). The sample was aligned to the rotation center, and a set of XRD patterns were collected at incremental steps of 0.25° over the maximum X-ray accessible ω range (36° or 50°) in a "step scan" mode. The fable software package (Sørensen et al., 2012) was used to process the spotty XRD patterns, and the orientation matrices of individual grains were determined using the GrainSpotter algorithm (Schmidt, 2014).

Table 1
Experimental conditions and results.

Run	P (GPa)[a]	T (K)	Phase assemblage by XRD
60 mol%MgSiO$_3$–30 mol%Al$_2$O$_3$–10 mol%Fe$_2$O$_3$–7 wt.% H$_2$O			
SH137	104(2)	1900(200)	Bdg $+\delta$
SH137[b]	94.1(2)	300 after quench	
SH172-a	109(2)	2000(200)	Bdg $+\delta$
SH172-a	99.0(2)	300 after quench	
S200u	109(2)	2120(200)	Bdg $+\delta$
S200u	111(2)	2400(200)	
S200u	102.4(2)	300 after quench	
Sb029	112(2)	1750(200)	Bdg+pPv $+\delta+$ py
Sb029	113(2)	2000(200)	
Sb029	115(2)	2300(200)	
Sb029	103.0(2)	300 after quench	
SH172-b	117(2)	2100(200)	Bdg+pPv $+\delta+$ py
SH172-b	106.5(2)	300 after quench	
Sb003	120(2)	2050(200)	pPv $+\delta+$ py
Sb003[b]	109.5(2)	300 after quench	
Sa032	123(2)	2050(200)	pPv $+\delta+$ py
Sa032	126(2)	2500(200)	pPv $+\delta$
Sa032	111.7(2)	300 after quench	
70 mol%MgSiO$_3$–30 mol%Al$_2$O$_3$–6 wt.% H$_2$O			
HS001	119(2)	2000(200)	Bdg $+$ pPv $+\delta$
HS001	108.1(2)	300 after quench	
AMG015-004[c]	128(1)	2190(100)	pPv $+\delta$
AMG015-004[c]	119.7(11)	300 after quench	

[a] Pressures are determined by thermal equation of state for Ne (Dewaele et al., 2008).

[b] Compositions of phases were measured (see Table 3).

[c] Data from Ohira et al. (2014). The py-phase is determined from the T-quenched XRD patterns by multigrain indexing.

2.4. TEM-EDS measurements

Complementary to the *in-situ* XRD characterization, *ex-situ* chemical analysis was performed on the recovered samples of Runs SH137 (phase assemblage: δ + Bdg) and Sb003 (phase assemblage: δ + py + pPv). The key for a successful recovery is to prepare a starting sample with low porosity and to release the Ne very slowly during decompression. We often recovered a whole sample inside the gasket hole. For these two recovered samples, we cannot distinguish the heated and unheated areas by texture in the SEM. A big heating spot with approximately 35×35 μm^2 was applied on the center of the sample, and we located the heating center based on the geometric center position (see Supporting Information, Fig. S3). In order to record the recovered phase assemblage in the heated area, we also collected a two-dimensional XRD scan under ambient conditions at 15U1, Shanghai Synchrotron Radiation Facility (SSRF). An FEI Versa-3D SEM coupled with a focused ion beam (FIB) system was used to cut and lift out a thin cross-section from the heating center (geometric center) in each of the recovered samples. Each thin section was polished to a thickness of approximately 60–100 nm using a focused Ga$^+$ ion beam. Chemical analysis was performed and elemental mapping images were obtained using an FEI Talos F200X field emission TEM operating at 200 kV and equipped with a SuperX EDS system. *Ex-situ* chemical analysis results were combined with *in-situ* XRD data to connect compositional changes with structural transformations (Zhang et al., 2019).

3. Results

3.1. Phase identification by XRD

Table 1 lists run conditions and phase assemblages identified by a combination of powder XRD and multigrain XRD. The phase relations in the MAFSH system were investigated at pressures ranging from 104 to 126 GPa and temperatures ranging from 1750
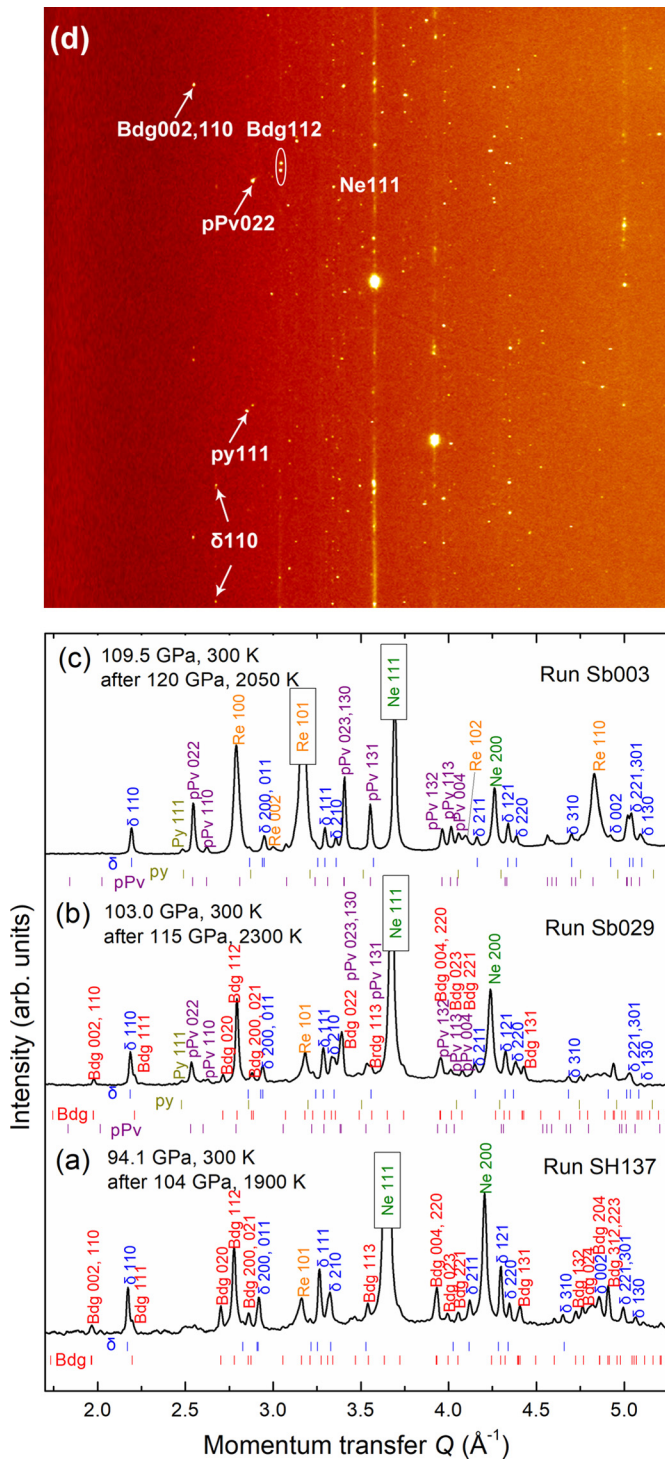
Fig. 2. Representative XRD patterns on the MAFSH sample at high P and after T quench. (a) Coexistence of bridgmanite (Bdg) and the δ-phase at 94 GPa and after T quench from heating at 1900 K. (b) Coexistence of Bdg, post-perovskite (pPv), pyrite (py) phase and δ-phase at 103 GPa after T quench from heating at 2150 K after 2150 K heating. (c) Coexistence of pPv, hydrous δ-phase and py-phase at 110 GPa after T quench from heating at 2050 K. (d) Portion of a two-dimensional "cake" image of Run Sb029. Unit-cell parameters of the coexisting phases are shown in Table 1. Panel c was shown in a previous study to demonstrate the experimental method (Zhang et al., 2019). The XRD patterns were background-subtracted. See the text for the detailed discussion.

to 2500 K. Selected powder XRD patterns of the phase assemblages after T quench are shown in Fig. 2. Fig. 2d shows a portion of a spotty two-dimensional XRD image of the run products of Run Sb029 after high P-T treatment. The original image in 2θ-η

polar coordination was converted into Cartesian coordinates. The δ-phase was present in all runs with a pronounced characteristic peak (110), which was partially overlapped with the peak (111) of the Bdg phase (if present). In contrast, the py-FeOOH$_x$ phase was only observed in the assemblages where the pPv phase was present. The characteristic peak (111) of the py-phase was occasionally invisible in the integrated XRD patterns at some rotation angles owing to its low concentration in the assemblage and grain growth after the heating treatment. As shown in Fig. 3, a weak peak (111) of the py-phase was present at $\omega = 0.8°$ but absent at $\omega = -1.2°$ in the integrated XRD patterns for Run Sb003. Detailed inspection of the XRD patterns (inset of Fig. 3) revealed that a few diffraction spots contributed to most of the intensity of the peak (111) at $\omega = 0.8°$. To identify such a minor phase, we applied the multigrain XRD to sort out 42 grains with 9–18 reflections confirmed for each grain (Run Sb003). A list of observed reflections of one selected grain of the py-phase is shown in Table S2.

3.2. Chemical analysis and elemental partitioning

We performed TEM analysis on two representative recovered samples of the δ + Bdg assemblage at 104 GPa and 1900 K (Run SH137) and the δ + py + pPv assemblage at 117 GPa and 2050 K (Run Sb003), respectively. The TEM elemental maps and phase distribution are shown in Fig. 4 and the chemical composition of individual phases in the assemblages are summarized in Table 2. In both samples, the silicate phase (Bdg or pPv) and the Al-rich δ-phase can be easily identified. In the Bdg-bearing assemblage (Run SH137), several small Fe-rich grains (Fig. 4a) with 30–80 nm in diameter were observed near the edge of the δ-phase grains. The composition of these Fe-rich grains cannot be resolved owing to the grain overlaps. We did not identify the py-phase in the Bdg-bearing assemblage from the high-pressure XRD pattern (Fig. 2a). Nish et al. (2017) showed that δ-phase (Fe$_{0.5}$Al$_{0.5}$)OOH cannot form complete solid solutions under ambient conditions; consequently, the quenched sample contains both individual Al-rich and Fe-rich (Fe,Al)OOH compounds. The Fe-rich grains in our Bdg-bearing assemblage might be formed as a result of exsolution of the Fe-rich component from the δ-phase during quenching. Another possibility is that the amount of py-phase in the Bdg-bearing assemblage is too low to be detected by XRD. In contrast, the py-phase FeOOH$_x$ was unambiguously identified using multigrain XRD in the pPv-bearing assemblage (Run Sb003) at high pressure, and the Fe–O grains (Fig. 4b) in the recovered pPv-bearing assemblage is a minor phase ($\sim$3 vol%) in TEM-EDS mapping image.

The chemical analysis revealed similar Al$_2$O$_3$ contents in the Bdg and pPv phases ($\sim$4 mol%) in both the assemblages, which was significantly lower than $\sim$19 mol% in the starting material. Previous studies reported that the Al$_2$O$_3$ partition coefficient [D(Al$_2$O$_3$) = Al$_2$O$_3$(mol% in δ-phase)/Al$_2$O$_3$ (mol% in Bdg or pPv)] was within the range of 14–26 throughout the lower mantle in the MASH system (Ohtani et al., 2018). In the Fe-bearing MAFSH system, we obtained an Al$_2$O$_3$ partition coefficient within 15–20 (Table 2), indicating that the addition of Fe to the system had a negligible effect on the partitioning behavior of Al. The Bdg phases in the mantle peridotite and MORB assemblages contained $\sim$5 and $\sim$15 wt.% Al$_2$O$_3$, respectively, under dry conditions (Irifune and Tsuchiya, 2015). Our experiments in a Fe-bearing system support the conclusion that the Al$_2$O$_3$ contents in Bdg could be reduced to $\sim$1 and $\sim$3 wt.% in the mantle peridotite and MORB assemblages, respectively, through selective partitioning of Al into the δ-phase (Ohtani et al., 2018).

The Fe$_2$O$_2$(OH)$_2$ contents in the δ-phase were $\sim$13 and $\sim$9 mol% in the Bdg-bearing and the pPv-bearing assemblages, respec-
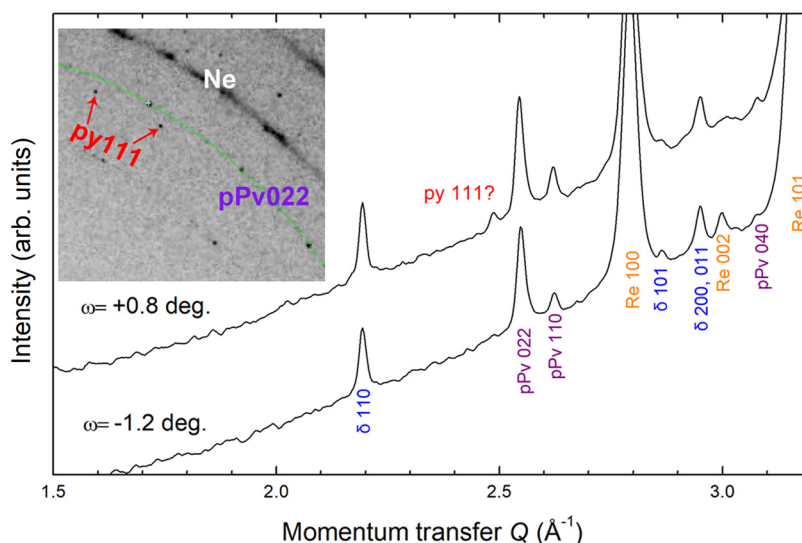
Fig. 3. Selected portions of the XRD patterns showing the weak py (111) at two close rotation angles (ω), respectively, in Run Sb003 after T quench. The inset shows that the diffraction image contains some diffraction spots, which contribute to most of the intensity of the weak peak observed in the integrated XRD pattern at $\omega = 0.8°$.

tively. We found that 8–9 mol% additional SiO_2 and 5–11 mol% $MgSiO_2(OH)_2$ were also incorporated into the δ-phases in both the assemblages. The results suggest that multiple substitution mechanisms, including $Al^{3+} + H^+ = Si^{4+}$ [$AlOOH = SiO_2$] (Litasov et al., 2007), $2Al^{3+} = Mg^{2+} + Si^{4+}$ [$Al_2O_2(OH)_2 = MgSiO_2(OH)_2$] (Ohira et al., 2014) and $Al^{3+} = Fe^{3+}$ [$AlOOH = FeOOH$] (Kawazoe et al., 2017), could be involved in the formation of the δ-phase. The composition of Bdg/pPv shows a slight enrichment of SiO_2 and depletion of MgO compared to the expected values from the stoichiometry. This may be due to a small amount of ferrous iron in Bdg/pPv. For simplicity, we assumed that all iron in the Bdg/pPv phase and δ-phase is in Fe^{3+}, and tentatively obtained an Fe_2O_3 partition coefficient [$D(Fe_2O_3) = Fe_2O_3$(mol% in δ-phase)/Fe_2O_3(mol% in Bdg or pPv)] within the range of 1–3. In other words, the Bdg/pPv phase remains iron-rich (mostly in Fe^{3+}) under hydrous conditions in the DLM.

3.3. Unit-cell volume versus composition

Based on the chemical analysis of the recovered samples, we can evaluate the relationship between chemical composition of the individual phases and their unit-cell volumes determined by *in-situ* XRD. In addition to the experiments performed on the MAFSH system, we also conducted one experiment on an Fe-free MASH sample (Run HS001) for comparison. As shown in Fig. 5a and Table 3, both the unit-cell volume of the δ-phase obtained in this study and the value reported by Ohira et al. (2014) are consistent with the EOS data for δ-AlOOH (Sano-Furukawa et al., 2009). This indicates that incorporation of 14 mol% $MgSiO_2(OH)_2$ into the δ-phase had negligible effect on its unit-cell volume. In contrast, the unit-cell volumes of the (Al,Fe)OOH δ-phase increase with increasing $Fe_2O_2(OH)_2$ content (Kawazoe et al., 2017; Nishi et al., 2017). In the present study, we measured the $Fe_2O_2(OH)_2$ content in the δ-phase is ∼13 mol% in Run SH137 and ∼9 mol% in Run Sb003, corresponding to volume differences of ∼1.0% and ∼0.7% relative to that of the δ-AlOOH phase, respectively. The chemical composition of the py-phase is simple: only Fe and O were detected in the TEM-EDS analysis. The unit-cell volume of the py-phase synthesized in this study (Fig. 5b) is comparable to that of the hydrous py-phase $FeOOH_x$ (Hu et al., 2016) or FeOOH (Nishi et al., 2017) but is approximately 10% larger than the py-phase FeO_2 (Hu et al., 2017), confirming the hydrous nature of the py-phase $FeOOH_x$ in the pPv-bearing assemblage.

Compositional effects on the Bdg and pPv phases have been intensively investigated (e.g., Ballaran et al., 2012; Catalli et al., 2009; Dorfman et al., 2013; Sun et al., 2018). Here, we used the reference EOS data of $Mg_{0.735}Fe_{0.21}Al_{0.07}Si_{0.965}O_3$ Bdg and pPv (denoted as Fe21Al7-Bdg and Fe21Al7-pPv, respectively) reported by Sun et al. (2018), the EOS data of $MgSiO_3$ pPv reported by Guignot et al. (2007) and those of single-crystal $MgSiO_3$ and $Mg_{0.60}Fe^{2+}_{0.03}Fe^{3+}_{0.38}Si_{0.62}Al_{0.36}O_3$ Bdgs (denoted as Fe41Al36-Bdg) reported by Ballaran et al. (2012). Based on the TEM-EDS analysis, the composition of the Bdg in Run SH137 and that of the pPv in Run Sb003 were estimated as $Mg_{0.80}Fe_{0.22}Si_{0.82}Al_{0.16}O_3$ (denoted as Fe22Al16-Bdg) and $Mg_{0.76}Fe_{0.32}Si_{0.78}Al_{0.14}O_3$ (denoted as Fe32Al14-pPv), respectively. As shown in Fig. 5c and Table 3, the unit-cell volumes of the Al-depleted Bdg and pPv phases in the Fe-free MASH system are slightly greater than those of pure $MgSiO_3$, and the unit-cell volume of Fe22Al16-Bdg in this study is ∼0.7% larger than that reported for Fe21Al7-Bdg by Sun et al. (2018), suggesting that Al incorporation into Bdg or pPv increases their volumes. The unit-cell volume of the Fe32Al14-pPv in the present study is ∼1.3% greater than that reported for Fe22Al16-pPv by Sun et al. (2018), indicating that incorporation of Fe^{3+} increases the volume of the pPv phase. In Run Sb029, in which the Bdg and pPv phases coexisted, we found that the unit-cell volume of the pPv phase is ∼0.7% larger than that of the coexisting Bdg, indicating a significantly higher Fe content in the pPv than that in the coexisting Bdg in the δ + py + Bdg + pPv assemblage (see the multigrain indexing of the Bdg and pPv individual grains in Tables S3 and S4, Supporting Information). Based on the relationship between the composition of the Bdg/pPv phases and the unit-cell volume (Table 2 and Table 3, respectively), we estimate that 1 at.% Fe content in Fe,Al-bearing Bdg and pPv increases the unit-cell volume by ∼0.14% and ∼0.19%, respectively. We then estimated the composition of the pPv phase with ∼21 at.% Fe coexisting with the Bdg phase with ∼9 at.% Fe in the Run Sb029. When the Bdg to pPv phase transition occurs in a hydrous system, we found that Fe preferentially partitions into the pPv phase over the coexisting Bdg phase by a factor of ∼2.

3.4. Phase relations and mass balance analysis

The coexisting phases are homogeneously distributed and the shapes of the coexisting phases are granular or polygonal as shown in the TEM-EDS images of the recovered sample (Fig. 4), indicat-
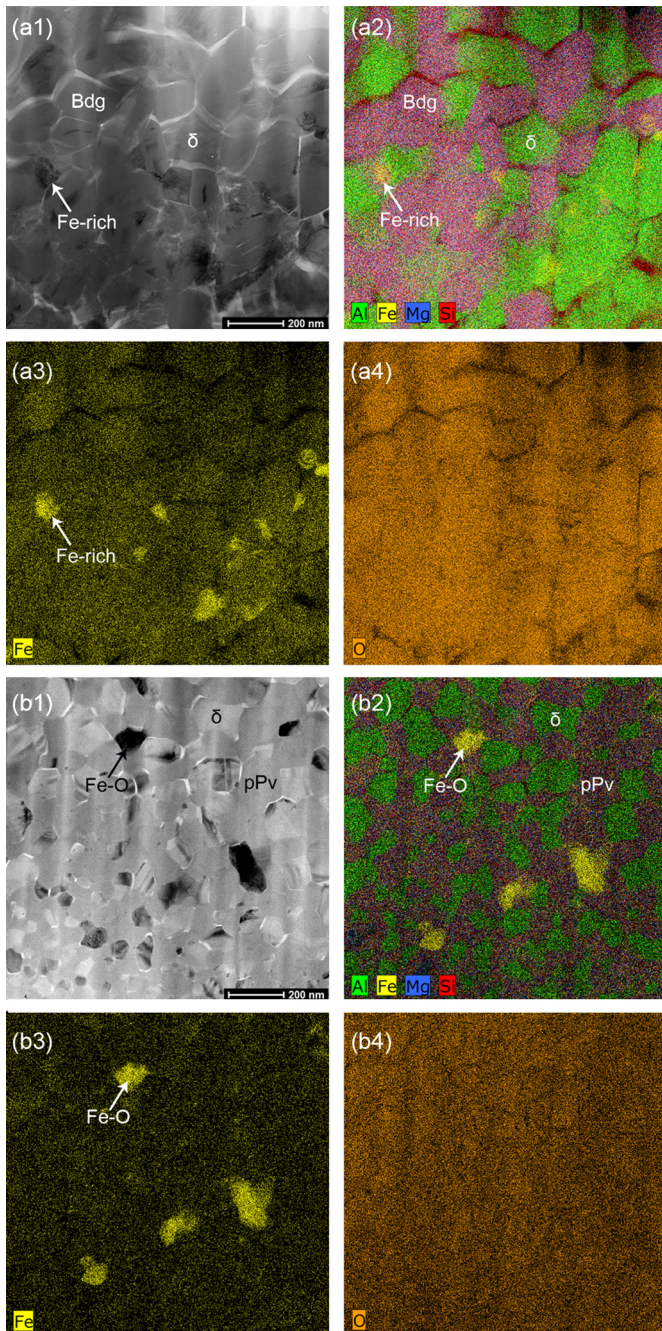
Fig. 4. TEM images and elemental maps of recovered samples (a) 104 GPa, 1900 K (Run SH137) and (b) 117 GPa, 2050 K (Run Sb003). Bright-field scanning TEM images are shown in panels a1 and b1. The compositional mapping images are shown: Al + Fe + Mg + Si (a2 and b2); Fe (a3 and b3); O (a4 and b4.) Elements Si, Mg, Al, Fe and O are shown in red, blue, green, yellow, orange, respectively. The chemical composition analysis results are given in Table 3. Fig. b2 and b3 were shown in a previous study to demonstrate the method (Zhang et al., 2019).

ing that the coexisting phases in the present experiments reached equilibrium or was very close to the equilibrium. On the basis of the TEM-EDS results for Runs SH137 and Sb003, we constructed the chemical compositions and tie lines between relevant phases in the chemographic diagrams (Fig. 6). The composition of the starting material is reasonably on the tie lines between the Bdg(pPv) and δ-phase (+py-phase) within the uncertainties. Table 2 shows a variation of around 10% in the composition of the individual phases in the assemblages, possibly caused by a temperature gradient during the heating. As it is difficult to determine

Table 2
Chemical compositions of coexisting phases at 104 GPa/1900 K for Run SH137 and at 117 GPa/2050 K for Run Sb003.

| Conditions	104 GPa/1900 K		117 GPa/2050 K	
	Bdg	δ-phase	pPv	δ-phase
Mg (at.%)	40.0(21)	5.6(10)	38.2(41)	2.6(19)
Si (at.%)	41.5(19)	10.2(18)	38.8(20)	6.9(26)
Al (at.%)	7.6(13)	70.3(19)	7.4(24)	81.4(35)
Fe (at.%)	10.9(20)	13.9(16)	15.5(30)	9.0(26)
N	14	18	10	8
Total	100.0	100.0	99.9	100.0
MgO (mol%)	44.0(23)	9.7(17)	43.2(46)	4.7(34)
SiO$_2$ (mol%)	45.8(21)	17.6(31)	43.9(22)	12.6(47)
Al$_2$O$_3$ (mol%)	4.2(7)	60.7(16)	4.2(14)	74.3(32)
Fe$_2$O$_3$ (mol%)[a]	6.0(22)	12.0(14)	8.7(17)	8.3(23)
Total	100.0	100.0	100.0	99.9
D(Al$_2$O$_3$)δ/Bdg or pPv	15(3)		20(7)	
D(Fe$_2$O$_3$)δ/Bdg or pPv	3(1)		1.0(5)	
δ-phase				
MgSiO$_2$(OH)$_2$ (mol%)		10.7(19)		4.9(36)
Al$_2$O$_2$(OH)$_2$ (mol%)		67.2(18)		78.1(34)
Fe$_2$O$_2$(OH)$_2$ (mol%)		13.3(16)		8.8(25)
SiO$_2$ (mol%)		8.7(15)		8.3(31)
Total	100.1	100.0	100.0	100.1

[a] Calculated as Fe$_2$O$_3$ for comparison.
The partition coefficients of D(Al$_2$O$_3$)δ/Bdg or pPv are defined as follows: D(Al$_2$O$_3$)δ/Bdg or pPv = Al$_2$O$_3$(mol% in δ-phase)/ Al$_2$O$_3$(mol% in Bdg or pPv). The partition coefficients of D(Fe$_2$O$_3$)δ/Bdg or pPv are defined as same as that of D(Al$_2$O$_3$)δ/Bdg or pPv. Numbers in parentheses represent uncertainties. N represents the number of analyses.

the disappearance of a minor py-phase at high temperature, we tentatively drew a boundary for the py-phase FeOOH$_x$ in Fig. 6. Considering the uncertainty of TEM-EDS measurements, we neglected the minor py-phase FeOOH$_x$ ($\sim$3 vol%) in the following mass balance analysis. On the basis of the Si and Al content, the mass balance calculation yields 64% Bdg + 36% δ and 70% pPv + 30% δ (+py) in the Bdg-bearing and pPv-bearing assemblages, respectively. Assuming stoichiometric compositions, $\sim$5 and $\sim$4 wt.% of water in the system can be stored in the Fe-bearing δ-phase in the Bdg-bearing and pPv-bearing assemblages, respectively. Apart from the water stored in the hydrous δ-phase, there is 2–3 wt.% excessive water in the MAFSH system. The excessive water may enter the Bdg/pPv lattice and/or form ice X at high pressures. However, we could not determine the water concentration in Bdg/pPv in our run products using synchrotron infrared spectroscopy and/or secondary ion mass spectrometry, because the Bdg/pPv grains are too small with grain size less than 200 nm. Furthermore, we could not rule out the possibility of partial water loss in the laser-heating experiments. Due to the experimental limitation, the present study shows preliminary results on the phase relations and mineral chemistry in an Fe,Al-bearing water-saturated system.

4. Geophysical implications

4.1. Water storage in Earth's deep lower mantle

Previous studies demonstrated that the δ-H solid solution AlOOH–MgSiO$_2$(OH)$_2$ is a stable water-carrier to the lowermost mantle along the normal mantle geotherm (Ohira et al., 2014; Walter et al., 2015). Walter et al. (2015) suggested that other components in the lower mantle such as Fe, Ca Na, K may lower the melting temperature relative to the MgO–Al$_2$O$_3$–SiO$_2$–H$_2$O system. Our results in a simplified basaltic composition show that incorporation of up to 13 mol% Fe$_2$O$_2$(OH)$_2$ and 9 mol% SiO$_2$ into the δ-phase did not reduce the thermal stability relative to
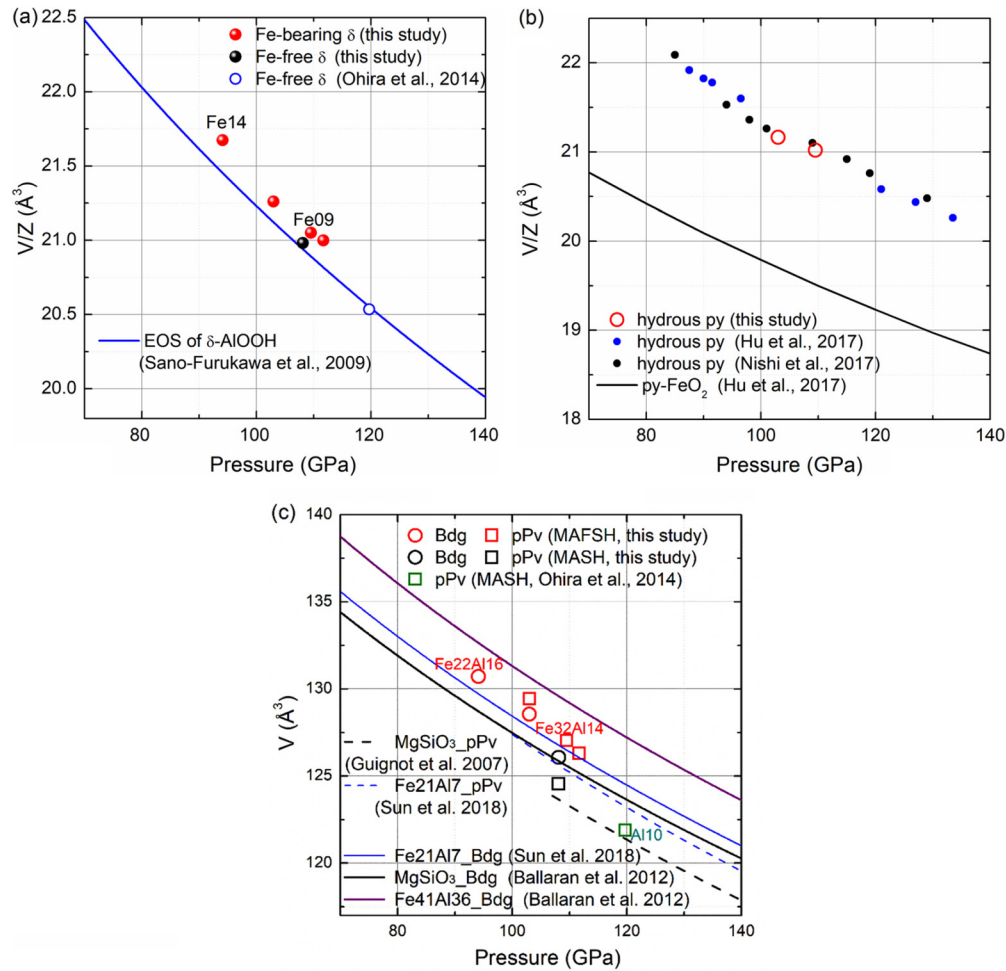
Fig. 5. Pressure–volume relations for (a) δ-phase, (b) py-phase, and (c) Bdg/pPv phase after T quench. Their lattice parameters are summarized in Table 3. The error bars of pressure and volume are within the data symbols. The abbreviations used here are the same as those in Fig. 1. In panel a, Fe14 and Fe09 represent the δ-phases containing 14 and 9 mol% $Fe_2O_2(OH)_2$, respectively. In panel c, Fe41Al36 represents Bdg with the chemical formula $Mg_{0.60}Fe^{2+}_{0.03}Fe^{3+}_{0.38}Si_{0.62}Al_{0.36}O_3$ from the study by Ballaran et al. (2012), Fe21Al7 represents $Mg_{0.735}Fe_{0.21}Al_{0.07}Si_{0.965}O_3$ Bdg or pPv from the study by Sun et al. (2018), and Fe22Al16 and Fe32Al14 represent $Mg_{0.80}Fe_{0.22}Si_{0.82}Al_{0.16}O_3$ Bdg and $Mg_{0.76}Fe_{0.32}Si_{0.78}Al_{0.14}O_3$ pPv determined in the present study, respectively.

that of the δ-H solid solution in the hydrous Fe-free system. The Fe-bearing δ-phase can carry water throughout the lower mantle along the normal mantle geotherm (Fig. 6). We observed the coexistence of the py-phase $FeOOH_x$, the Fe-rich pPv phase, and the δ-phase along a cold geotherm (Brown and Shankland, 1981; Kirby et al., 1996) (Fig. 6, blue empty circles), indicating that the py-phase $FeOOH_x$ could be a potential water carrier subducted into the D'' layer. The calculation by Muir and Brodholt (2018) shows that a large amount of water (>1000 ppm) may be needed to stabilize the hydrous δ-phase, and water may create significant number of vacancies in Bdg in the deepest lower mantle in the $MgO–Al_2O_3–SiO_2–H_2O$ system. In addition to the hydrous δ-phase and the py-phase, the aluminous Bdg could be a possible water reservoir in the DLM. Addition of iron in the system can further complicate the water partitioning behavior between the δ-phase and the Bdg/pPv phase and future studies are desired to clarify the partitioning behavior of water under the conditions of the lower mantle.

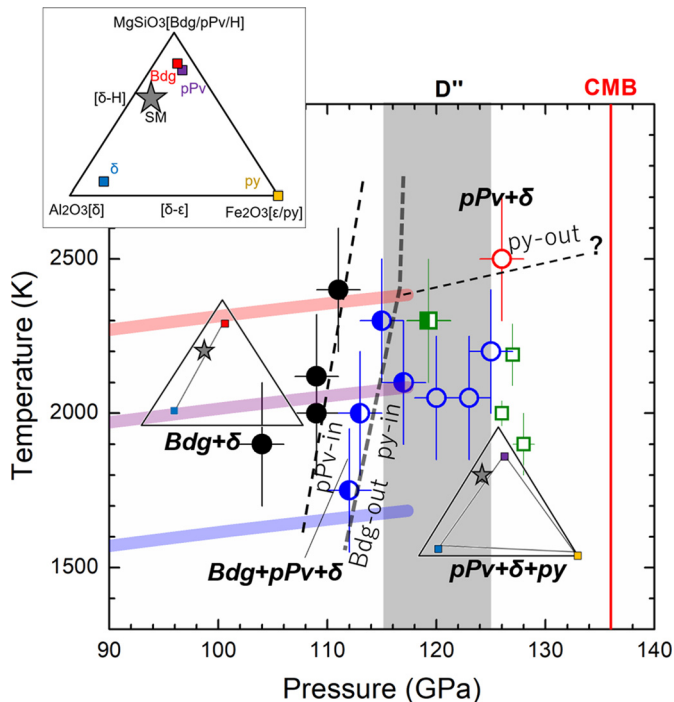### 4.2. Interpretation of seismic heterogeneities by hydrous slabs subducted in the D'' layer

The CMB is a thermal boundary between the solid mantle and liquid outer core, and the composition and structure of the lowermost mantle is complex because it is believed to be the graveyard

of subducting slabs as well as the source region of hot plumes (van der Hilst et al., 2007). In reconciling the Bdg to pPv transition with the D" seismic velocity discontinuity, we investigated the stability and element partitioning in the phase assemblages. In spite of the qualitative nature of the phase boundary determination in the present experiments, the P-T diagram clearly showed that the thickness of the Bdg to pPv phase transition in the MAFSH system is $\sim 150 \pm 75$ km ($\sim 8 \pm 4$ GPa) at ~ 2000 K (along the cold slab in Fig. 6), considerably narrower than the wide transition thickness of 400–600 km (25–30 GPa) in the fixed Fe,Al-bearing compositions (Catalli et al., 2009; Sun et al., 2018). Al depletion in both the pPv and Bdg phases should be responsible for the much narrower transition boundary obtained in the present study. Hirose et al. (2005) reported a significant increase in the Fe/(Mg+Fe) atomic ratio from 0.23 to 0.40 across the Bdg to pPv transition while the Al/Si ratio remains unchanged at 0.39 in the MORB composition. We used an Al-enriched starting material with an atomic ratio of Al/Si = 1 to enhance the diffraction of the δ-phase compared with Al/Si ≈ 0.35 in a natural MORB starting composition. Applying the partitioning coefficients obtained in the present study, the Al_2O_3 content in both the Bdg and pPv phases can be further reduced from the current value of ~ 4 mol% to 1–2 mol% in basaltic subducted slabs, and the transition thickness can be reduced accordingly. Moreover, the Fe content is more enriched in pPv (~ 21 at.%) than that in the coexisting Bdg (~ 9 at.%) (Run Sb029), and thus the Bdg to

Table 3

Phase assemblages and lattice parameters determined by the nonlinear least-squares fitting method after multigrain or powder XRD indexation at 300 K.

Run	Phase	N/n[a]	a (Å)	b (Å)	c (Å)	V (Å)	P (GPa)[b]
60 mol%MgSiO$_3$–30 mol%Al$_2$O$_3$–10 mol%Fe$_2$O$_3$–7 wt.% H$_2$O							
SH137	Ne	–	2.9869(4)	–	–	–	94.1(2)
(1900 K)	Bdg	93/3	4.3924(3)	4.6492(4)	6.4007(12)	130.71(2)	–
	δ	64/4	4.3174(6)	3.8840(5)	2.5852(3)	43.350(6)	–
Sb029	Ne	–	2.9631(5)	–	–	–	103.0(2)
(2300 K)	Bdg	136/2	4.3652(5)	4.6304(2)	4.6304(2)	128.55(1)	–
	pPv	61/3	2.5273(4)	8.2176(14)	6.2326(6)	129.44(2)	–
	δ	60/4	4.2888(7)	3.8735(5)	2.5596(2)	42.522(6)	–
	py	87/4	4.3909(2)	–	–	84.654(9)	–
Sb003	Ne	–	2.9470(6)	–	–	–	109.5(2)
(2050 K)	pPv	73/4	2.5067(2)	8.0044(12)	6.2052(15)	127.03(2)	–
	δ	41/4	4.2736(10)	3.8594(9)	2.5526(4)	42.101(9)	–
	py	33/3	4.3808(3)	–	–	84.08(2)	–
Sa200u	Ne	–	2.9648(5)	–	–	–	102.4(2)
(2200 K)	Bdg	187/2	4.3586(2)	4.6357(5)	6.3813(4)	128.93(1)	–
Sa032	Ne	–	2.9419(5)	–	–	–	111.7(2)
(2500 K)	pPv	83/3	2.5026(2)	8.1512(8)	6.1913(7)	126.30(1)	–
	δ	43/2	4.2687(5)	3.8553(6)	2.5523(3)	42.00(1)	–
70 mol%MgSiO$_3$–30 mol%Al$_2$O$_3$–6 wt.% H$_2$O							
HS001	Ne	–	2.9507(5)	–	–	–	108.1(2)
(2000 K)	Bdg	83/3	4.3388(4)	4.5963(7)	6.3217(5)	126.07(1)	–
	pPv	85/5	2.4817(2)	8.1505(6)	6.1575(6)	124.55(1)	–
	δ	44/4	4.2711(5)	3.8513(7)	2.5541(4)	42.014(7)	–
AMG015-004[c]	pPv	–	2.4667(7)	8.0726(18)	6.1216(10)	121.90(9)	119.7(11)
(2190)	δ	–	4.2451(4)	3.8260(3)	2.5292(2)	41.07(2)	–

[a] N is the number of reflections in total; n is the number of merged grains.
[b] P represents the pressure (Ne scale) after temperature was quenched to room temperature.
[c] Data from Ohira et al. (2014).

Fig. 6. *P-T* diagram showing the phase relations under the conditions of the DLM. Broad translucent lines are suggested geotherms for very cold slab (blue), cold slab (purple) and normal mantle (red) (Brown and Shankland, 1981; Kirby et al., 1996). The gray shadowed region represents the *P* range of the D″ seismic discontinuity. The solid red line represents the depth of the core–mantle boundary. Solid, half-filled, and empty symbols represent run products containing Bdg, Bdg+pPv, and pPv, respectively. Black: Fe-bearing system containing the δ-phase; blue: Fe-bearing system containing the δ-phase and the py-phase; green: Fe-free system containing the δ-phase ("pPv +δ" data from Ohira et al., 2014). Chemographies show the two different phase assemblages stable at 104 GPa, 1900 K and 120 GPa, 2050 K from the TEM-EDS results. Possible relevant tie lines between phases are shown. SM = starting material; δ-ε = AlOOH–FeOOH solid solutions; δ-H = AlOOH–Mg$_{0.5}$Si$_{0.5}$OOH solid solutions.

from subducting oceanic slabs impinging on the CMB (Ren et al., 2007). The presence of partial melt above the CMB is a candidate for producing the ULVZs (Andrault et al., 2012). The hydrous Fe-bearing hydrous phases would eventually dehydrate at the base of the lower mantle due to a steep temperature increase and water released from dehydration might trigger partial melting and produce the seismic features of the ULVZs.

Acknowledgements

pPv phase transition can occur at a depth corresponding to the D″ discontinuity. If the hydrous Fe,Al-bearing basaltic compositions survive in slabs subducted to the DLM region, the Bdg to pPv transition can provide a valid interpretation for the D″ discontinuity (Lay, 2008). The ULVZs are distributed regionally at the base of the D″ layer. The source of the ULVZs may require distinct chemical compositions with lower melting temperatures, i.e., materials

Appendix A. Supplementary material

Supplementary material related to this article can be found online at https://doi.org/10.1016/j.epsl.2019.115714.

References

Andrault, D., Petitgirard, S., Lo Nigro, G., Devidal, J.-L., Veronesi, G., Garbarino, G., Mezouar, M., 2012. Solid–liquid iron partitioning in Earth's deep mantle. Nature 487, 354–357. https://doi.org/10.1038/nature11294.

Ballaran, T.B., Kurnosov, A., Glazyrin, K., Frost, D.J., Merlini, M., Hanfland, M., Caracas, R., 2012. Effect of chemistry on the compressibility of silicate perovskite in the lower mantle. Earth Planet. Sci. Lett. 333–334, 181–190. https://doi.org/10.1016/j.epsl.2012.03.029.

Brown, J.M., Shankland, T.J., 1981. Thermodynamic parameters in the Earth as determined from seismic profiles. Geophys. J. Int. 66, 579–596. https://doi.org/10.1111/j.1365-246X.1981.tb04891.x.

Catalli, K., Shim, S.-H., Prakapenka, V., 2009. Thickness and Clapeyron slope of the post-perovskite boundary. Nature 462, 782–785. https://doi.org/10.1038/nature08598.

Dewaele, A., Datchi, F., Loubeyre, P., Mezouar, M., 2008. High pressure-high temperature equations of state of neon and diamond. Phys. Rev. B, Condens. Matter Mater. Phys. 77, 1–9. https://doi.org/10.1103/PhysRevB.77.094106.

Dorfman, S.M., Meng, Y., Prakapenka, V.B., Duffy, T.S., 2013. Effects of Fe-enrichment on the equation of state and stability of (Mg, Fe)SiO$_3$ perovskite. Earth Planet. Sci. Lett. 361, 249–257. https://doi.org/10.1016/j.epsl.2012.10.033.

Duan, Y., Sun, N., Wang, S., Li, X., Guo, X., Ni, H., Prakapenka, V.B., Mao, Z., 2018. Phase stability and thermal equation of state of δ-AlOOH: implication for water transportation to the Deep Lower Mantle. Earth Planet. Sci. Lett. 494, 92–98. https://doi.org/10.1016/j.epsl.2018.05.003.

Dziewonski, A.M., Anderson, D.L., 1981. Preliminary reference Earth model. Phys. Earth Planet. Inter. 25, 297–356. https://doi.org/10.1016/0031-9201(81)90046-7.

Frost, D.J., Liebske, C., Langenhorst, F., McCammon, C.a., Tronnes, R.G., Rubie, D.C., 2004. Experimental evidence for the existence of iron-rich metal in the Earth's lower mantle. Nature 428, 409–412. https://doi.org/10.1029/200/JC000964.

Grocholski, B., Catalli, K., Shim, S., Prakapenka, V., 2012. Mineralogical effects on the detectability of the postperovskite boundary. Proc. Natl. Acad. Sci. USA 109, 2275–2279. https://doi.org/10.1073/pnas.1109204109.

Guignot, N., Andrault, D., Morard, G., Bolfan-Casanova, N., Mezouar, M., 2007. Thermoelastic properties of post-perovskite phase MgSiO$_3$ determined experimentally at core-mantle boundary P-T conditions. Earth Planet. Sci. Lett. 256, 162–168. https://doi.org/10.1016/j.epsl.2007.01.025.

Hamilton, D.L., Henderson, C.M.B., 1968. The preparation of silicate compositions by a gelling method. Mineral. Mag. 36, 832–838. https://doi.org/10.1180/minmag.1968.036.282.11.

Hirose, K., Takafuji, N., Sata, N., Ohishi, Y., 2005. Phase transition and density of subducted MORB crust in the lower mantle. Earth Planet. Sci. Lett. 237, 239–251. https://doi.org/10.1016/j.epsl.2005.06.035.

Hu, Q., Kim, D.Y., Liu, J., Meng, Y., Yang, L., Zhang, D., Mao, W.L., Mao, H., 2017. Dehydrogenation of goethite in Earth's deep lower mantle. Proc. Natl. Acad. Sci. 114, 1498–1501. https://doi.org/10.1073/pnas.1620644114.

Hu, Q., Kim, D.Y., Yang, W., Yang, L., Meng, Y., Zhang, L., Mao, H.-K., 2016. FeO$_2$ and FeOOH under deep lower-mantle conditions and Earth's oxygen–hydrogen cycles. Nature 534, 241–244. https://doi.org/10.1038/nature18018.

Irifune, T., Tsuchiya, T., 2015. Phase Transitions and Mineralogy of the Lower Mantle, Treatise on Geophysics, second edition. Elsevier B.V.

Kárason, H., van der Hilst, R.D., 2000. Constraints on Mantle Convection from Seismic Tomography, pp. 277–288.

Kawazoe, T., Ohira, I., Ishii, T., Ballaran, T.B., McCammon, C., Suzuki, A., Ohtani, E., 2017. Single crystal synthesis of δ-(Al, Fe)OOH. Am. Mineral. 102, 1953–1956. https://doi.org/10.2138/am-2017-6153.

Kirby, S.H., Stein, S., Okal, E.A., Rubie, D.C., 1996. Metastable mantle phase transformations and deep earthquakes in subducting oceanic lithosphere. Rev. Geophys. 34, 261–306. https://doi.org/10.1029/96RG01050.

Lay, T., 2008. Sharpness of the D$''$ discontinuity beneath the Cocos plate: implications for the perovskite to post-perovskite phase transition. Geophys. Res. Lett. 35, 1–5. https://doi.org/10.1029/2007GL032465.

Litasov, K.D., Kagi, H., Shatskiy, A., Ohtani, E., Lakshtanov, D.L., Bass, J.D., Ito, E., 2007. High hydrogen solubility in Al-rich stishovite and water transport in the lower mantle. Earth Planet. Sci. Lett. 262, 620–634. https://doi.org/10.1016/j.epsl.2007.08.015.

Mao, H., Hu, Q., Yang, L., Liu, J., Kim, D.Y., Meng, Y., Zhang, L., Prakapenka, V.B., Yang, W., Mao, W.L., 2017. When water meets iron at Earth's core-mantle boundary. Natl. Sci. Rev., 1–9. https://doi.org/10.1093/nsr/nwx109.

Meng, Y., Hrubiak, R., Rod, E., Boehler, R., Shen, G., 2015. New developments in laser-heated diamond anvil cell with in situ synchrotron x-ray diffraction at High Pressure Collaborative Access Team. Rev. Sci. Instrum. 86, 072201. https://doi.org/10.1063/1.4926895.

Muir, J.M.R., Brodholt, J.P., 2018. Water distribution in the lower mantle: implications for hydrolytic weakening. Earth Planet. Sci. Lett. 484, 363–369. https://doi.org/10.1016/j.epsl.2017.11.051.

Murakami, M., 2004. Post-perovskite phase transition in MgSiO$_3$. Science 80 (304), 855–858. https://doi.org/10.1126/science.1095932.

Nishi, M., Irifune, T., Tsuchiya, J., Tange, Y., Nishihara, Y., Fujino, K., Higo, Y., 2014. Stability of hydrous silicate at high pressures and water transport to the deep lower mantle. Nat. Geosci. 7, 224–227. https://doi.org/10.1038/ngeo2074.

Nishi, M., Kuwayama, Y., Tsuchiya, J., Tsuchiya, T., 2017. The pyrite-type high-pressure form of FeOOH. Nature 547, 205–208. https://doi.org/10.1038/nature22823.

Oganov, A.R., Ono, S., 2004. Theoretical and experimental evidence for a post-perovskite phase of MgSiO$_3$ in Earth's D$''$ layer. Nature 430, 445–448. https://doi.org/10.1038/nature02701.

Ohira, I., Ohtani, E., Sakai, T., Miyahara, M., Hirao, N., Ohishi, Y., Nishijima, M., 2014. Stability of a hydrous δ-phase, AlOOH–MgSiO$_2$(OH)$_2$, and a mechanism for water transport into the base of lower mantle. Earth Planet. Sci. Lett. 401, 12–17. https://doi.org/10.1016/j.epsl.2014.05.059.

Ohta, K., Hirose, K., Lay, T., Sata, N., Ohishi, Y., 2008. Phase transitions in pyrolite and MORB at lowermost mantle conditions: implications for a MORB-rich pile above the core–mantle boundary. Earth Planet. Sci. Lett. 267, 107–117. https://doi.org/10.1016/j.epsl.2007.11.037.

Ohtani, E., 2015. Hydrous minerals and the storage of water in the deep mantle. Chem. Geol. 418, 6–15. https://doi.org/10.1016/j.chemgeo.2015.05.005.

Ohtani, E., Litasov, K., Suzuki, A., Kondo, T., 2001. Stability field of new hydrous phase, for water transport into the deep mantle. Geophys. Res. Lett. 28, 3991–3993.

Ohtani, E., Yuan, L., Ohira, I., Shatskiy, A., Litasov, K., 2018. Fate of water transported into the deep mantle by slab subduction. J. Asian Earth Sci. 167, 2–10. https://doi.org/10.1016/j.jseaes.2018.04.024.

Pearson, D.G., Brenker, F.E., Nestola, F., McNeill, J., Nasdala, L., Hutchison, M.T., Matveev, S., Mather, K., Silversmit, G., Schmitz, S., Vekemans, B., Vincze, L., 2014. Hydrous mantle transition zone indicated by ringwoodite included within diamond. Nature 507, 221–224. https://doi.org/10.1038/nature13080.

Prakapenka, V.B., Kubo, A., Kuznetsov, A., Laskin, A., Shkurikhin, O., Dera, P., Rivers, M.L., Sutton, S.R., 2008. Advanced flat top laser heating system for high pressure research at GSECARS: application to the melting behavior of germanium. High Press. Res. 28, 225–235. https://doi.org/10.1080/08957950802050718.

Ren, Y., Stutzmann, E., van der Hilst, R.D., Besse, J., 2007. Understanding seismic heterogeneities in the lower mantle beneath the Americas from seismic tomography and plate tectonic history. J. Geophys. Res., Solid Earth 112, 1–15. https://doi.org/10.1029/2005JB004154.

Sano-Furukawa, A., Kagi, H., Nagai, T., Nakano, S., Fukura, S., Ushijima, D., Iizuka, R., Ohtahtahtani, E., Yagi, T., 2009. Change in compressibility of δ-AlOOH and δ-AlOOD at high pressure: a study of isotope effect and hydrogen-bond symmetrization. Am. Mineral. 94, 1255–1261. https://doi.org/10.2138/am.2009.3109.

Sano, A., Ohtani, E., Kondo, T., Hirao, N., Sakai, T., Sata, N., Ohishi, Y., Kikegawa, T., 2008. Aluminous hydrous mineral δ-AlOOH as a carrier of hydrogen into the core-mantle boundary. Geophys. Res. Lett. 35, 1–5. https://doi.org/10.1029/2007GL031718.

Schmidt, S., 2014. GrainSpotter: a fast and robust polycrystalline indexing algorithm. J. Appl. Crystallogr. 47, 276–284. https://doi.org/10.1107/S1600576713030185.

Sørensen, H.O., Schmidt, S., Wright, J.P., Vaughan, G.B.M., Techert, S., Garman, E.F., Oddershede, J., Davaasambu, J., Paithankar, K.S., Gundlach, C., Poulsen, H.F., 2012. Multigrain crystallography. Z. Kristallogr. 227, 63–78. https://doi.org/10.1524/zkri.2012.1438.

Sun, N., Wei, W., Han, S., Song, J., Li, X., Duan, Y., Prakapenka, V.B., Mao, Z., 2018. Phase transition and thermal equations of state of (Fe, Al)-bridgmanite and post-perovskite: implication for the chemical heterogeneity at the lowermost mantle. Earth Planet. Sci. Lett. 490, 161–169. https://doi.org/10.1016/j.epsl.2018.03.004.

Suzuki, A., Ohtani, E., Kamada, T., 2000. A new hydrous phase δ-AlOOH synthesized at 21 GPa and 1000 C. Phys. Chem. Miner. 27, 689–693. https://doi.org/10.1007/s002690000120.

Tschauner, O., Huang, S., Greenberg, E., Prakapenka, V.B., Ma, C., Rossman, G.R., Shen, A.H., Zhang, D., Newville, M., Lanzirotti, A., Tait, K., 2018. Ice-VII inclusions in diamonds: evidence for aqueous fluid in Earth's deep mantle. Science 80 (359), 1136–1139. https://doi.org/10.1126/science.aao3030.

van der Hilst, R.D., 1999. Compositional heterogeneity in the bottom 1000 kilometers of Earth's mantle: toward a hybrid convection model. Science 283, 1885–1888. https://doi.org/10.1126/science.283.5409.1885.

van der Hilst, R.D., de Hoop, M.V., Wang, P., Shim, S.-H., Ma, P., Tenorio, L., 2007. Seismostratigraphy and thermal structure of Earth's core-mantle boundary region. Science 315, 1813–1817. https://doi.org/10.1126/science.1137867.

Walter, M.J., Thomson, A.R., Wang, W., Lord, O.T., Ross, J., McMahon, S.C., Baron, M.A., Melekhova, E., Kleppe, A.K., Kohn, S.C., 2015. The stability of hydrous

silicates in Earth's lower mantle: experimental constraints from the systems $MgO–SiO_2–H_2O$ and $MgO–Al_2O_3–SiO_2–H_2O$. Chem. Geol. 418, 16–29. https://doi.org/10.1016/j.chemgeo.2015.05.001.

Yuan, L., Ohtani, E., Ikuta, D., Kamada, S., Tsuchiya, J., Naohisa, H., Ohishi, Y., Suzuki, A., 2018. Chemical reactions between Fe and H_2O up to megabar pressures and implications for water storage in the Earth's mantle and core. Geophys. Res. Lett. 45, 1330–1338. https://doi.org/10.1002/2017GL075720.

Zhang, L., Popov, D., Meng, Y., Wang, J., Ji, C., Li, B., Mao, H., 2016. In-situ crystal structure determination of seifertite SiO_2 at 129 GPa: studying a minor phase near Earth's core–mantle boundary. Am. Mineral. 101, 231–234. https://doi.org/10.2138/am-2016-5525.

Zhang, L., Yuan, H., Meng, Y., Mao, H., 2019. Development of high-pressure multigrain X-ray diffraction for exploring the Earth's interior. Engineering. https://doi.org/10.1016/j.eng.2019.02.004.

Zhang, L., Yuan, H., Meng, Y., Mao, H., 2018. Discovery of a hexagonal ultradense hydrous phase in (Fe, Al)OOH. Proc. Natl. Acad. Sci. 115, 2908–2911. https://doi.org/10.1073/pnas.1720510115.

Zhao, D., 2012. Tomography and dynamics of western-pacific subduction zones. Monogr. Environ. Earth Planets 1, 1–70. https://doi.org/10.5047/meep.2012.00101.0001.